Phage display against two-dimensional metal-organic nanosheets as a new route to highly selective biomolecular recognition surfaces

Amelia C. Wood, Edwin C. Johnson, Ram R. R. Prasad, Mark V. Sullivan, Nicholas W. Turner, Steven P. Armes, Sarah S. Staniland, Jonathan A. Foster

Dainton Building, Department of Chemistry, University of Sheffield, Brook Hill, Sheffield S3 7HF, UK

KEYWORDS. Phage Display, Metal-Organic Nanosheet, Biopanning, Quartz-crystal microbalance, Surface Plasmon Resonance

ABSTRACT: Peptides are important biomarkers for a range of diseases, however distinguishing different amino-acid sequences using artificial receptors remains a major challenge in biomedical sensing. Here we present a new approach to creating highly selective recognition surfaces using phage display biopanning against metal-organic nanosheets (MONs) and demonstrate their use as the next-generation of biomolecular recognition surfaces. Three MONs (ZIF-7, ZIF-7-NH_2 and Hf-BTB-NH_2) were chosen as initial targets to demonstrate how simple synthetic modifications can enhance selectivity towards specific amino acid sequences. Each MON system was added to a solution containing every possible combination of 7-residue peptides attached to bacteriophage hosts and the highest affinity binding peptides for each system was identified via successive biopanning rounds. In each case only a single peptide sequence was isolated (YNYRNLL – ZIF-7, NNWWAPA – ZIF-7-NH_2 and FTVRDLS – Hf-BTB-NH_2). This indicates that these MONs are highly selective, which is attributed to their 2D nanosheet structure. Zeta potential and contact angle measurements were conducted on each MON and combined with calculated properties for the peptide sequences and binding studies to provide insights into the relative importance of electrostatic, hydrophobic and co-ordination bonding interactions. A quartz crystal microbalance (QCM) was used to model phage binding and the Hf-BTB-NH_2 MON coated QCM produced a 5-fold higher signal for FTVRDLS functionalised phage compared to phage with generic peptide sequences. Further studies focusing on Hf-BTB-NH_2 confirmed that the VRDL sequence was highly conserved, and on-target binding exhibited equilibrium dissociation constants that are comparable to natural recognition materials. Surface plasmon resonance (SPR) studies indicated a 4600-fold higher equilibrium dissociation constant (K_D) for FTVRDLS compared to those obtained for off-target sequences, comparable to those of antibodies ($K_D = 4 \times 10^{-10}$). We anticipate that the highly tunable nature of MONs will enhance our understanding of binding interactions and enable molecular recognition of biomedically important peptides.

INTRODUCTION

Complex surface structures are responsible for the remarkable degree of biomolecular selectivity found in nature. Macromolecules bind to these bio-interfaces through multiple weak interactions, with electrostatic and hydrophobic interactions critical in determining selectivity.[1] Two-dimensional materials represent promising artificial mimics due to their high specific surface areas and accessible functional groups.[2,3] A wide range of nanomaterials including transition metal dichalcogenides, MXenes and graphene have displayed an ability to bind biological macromolecules such as proteins and DNA.[4–6] However, the simple inorganic structure of these surfaces leads to stochastic functionalization with different binding groups, therefore limiting their selectivity.

Metal-organic framework nanosheets (MONs) are a class of two-dimensional materials that combine organic ligands with metal nodes.[7,8] The modular structure of MONs enables systematic tuning of surface chemistry without changing the overall topology, while their crystalline nature affords a periodic array of recognition sites that promotes multidentate binding.[9] Presentation of these functional groups on the surface of the nanosheets, rather than within the pores of a three-dimensional metal-organic framework (MOF), removes any size limitations.[10] Early generations of MON-based biosensors have typically involved fluorescence quenching of dye-labeled single-stranded DNA, functionalization with bioreceptors and nanozyme behavior.[3,11–16] In these examples, much of the sensitivity and selectivity is conferred by other components, such as aptamers and antibodies, enzymes, nanoparticles or other two-dimensional materials.[9]

To the best of our knowledge, there are currently no studies investigating the interaction of specific sequences of amino acids with MONs, although several studies have investigated their interactions with their three-dimensional analogs, MOFs. Indeed, several MOFs are promising catalysts

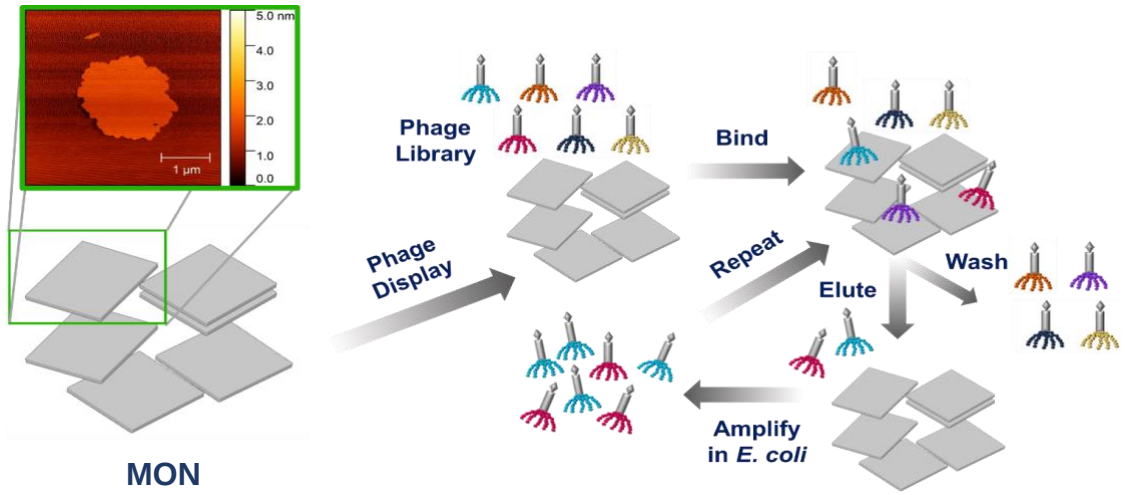

Figure 1: Schematic illustration of phage display against MONs (inset AFM image shows ZIF-7-NH_2), which includes phage incubation with MON to encourage binding, washing and elution steps, and phage amplification using *E. coli.*

for the formation and cleavage of peptides, as well as the selective hydrolysis of proteins.[17–20] Parac-Vogt and co-workers investigated the adsorption of a diverse range of dipeptides onto various Zr-based MOFs. Extensive screening revealed that affinity depended on hydrophobic, aromatic and cation–π interactions arising from the hydrophobic/aromatic nature of the linkers and cluster connectivity.[21] However, the diversity of both MOFs and peptide sequences and the complexity of their interactions means that identifying strong-binding combinations for use as highly selective biomolecular recognition surfaces remains a formidable challenge.

Phage display biopanning provides an alternative approach to exploring peptide-substrate interactions.[22,23] A library of bacteriophages presenting various combinations of peptides are incubated with a given target under competitive binding conditions to identify the most strongly binding sequences (Figure 1). This approach has been used to interrogate antigen-antibody interactions through epitope mapping as well as to identify suitable peptides for bioinspired mineralization.[24–26] In particular, Fan and co-workers used phage display to identify strongly binding peptides to a series of water-stable MOFs, which they used to control nucleation, modify their surface properties and tune the release of cargo.[27]

We hypothesized that biopanning could be used to identify strongly binding peptide sequences and hence design highly selective MON based biomolecular recognition surfaces for biomedical applications. Three different two-dimensional MON systems (ZIF-7, ZIF-7-NH_2 and Hf-BTB-NH_2) were selected to explore the effect of subtly different components on biomolecular recognition performance. Phage display was utilized to determine which peptides would exhibit strong binding to the surface of each MON out of a library of 1×10^{13} possible combinations of 7 amino acids. In each case, a consensus binding peptide sequence with strong affinity to its nanosheet system was identified, highlighting the intrinsic bio-selectivity of these ultrathin MONs. A study of MON-functionalized quartz-crystal microbalance (QCM) sensor exhibited a 5-fold increase in signal for the selective peptide functionalized phage compared to generic peptide sequences for the Hf-BTB-NH_2 system. Subsequently, we investigated the peptide sensitivity of Hf-BTB-NH_2 MONs using SPR analysis. This technique indicated a remarkably high equilibrium dissociation constant (K_D) of 4.15×10^{-10} ($\pm 0.32 \times 10^{-10}$) was observed for on-target interactions which is comparable to naturally occurring biomolecular recognition components such as antibodies.[28] Overall, our results demonstrate that specific peptide sequences can exhibit strong selective binding to MONs opening up a new route to the design of next-generation biomolecular recognition surfaces.

RESULTS AND DISCUSSION

Synthesis and characterization of layered MOFs and their exfoliation to form MONs. Three layered MOFs, chosen for their aqueous stability and differences in their chemical structure, were synthesized and exfoliated to form nanosheets.

The first system, ZIF-7 (Figure 2d), has previously been reported by a number of groups and used for gas separation, solid-phase extraction, and membrane filtration.[29–31] Here we adapted a method developed by Liu *et al*. and Peng *et al*. for its synthesis.[32,33] Benzimidazole and zinc nitrate hexahydrate were reacted under ambient conditions in DMF to produce a 3D ZIF-7-I phase material prior to refluxing in water to induce a hydrothermal phase transition that resulted in the bulk layered phase, ZIF-7-III (Figure S1). X-ray powder diffraction (XRPD) pattern of the resulting white microcrystalline powder matched that of the predicted ZIF-7-III pattern (Figure 2i) while scanning electron microscopy (SEM) studies also confirmed the formation of the layered material (Figure 2a).

Liquid exfoliation was achieved through ultrasonication of layered ZIF-7-III for 2 h in a 1:1 methanol/*n*-propanol mixture. Ultrathin nanosheets of 0.6 nm mean height and approximately 630 nm length were obtained, as indicated by atomic force microscopy (AFM) images (Figure 2e and Figure S18). Dynamic light scattering (DLS) reported a spherical equivalent diameter of 1063 nm (Figure S21).

The second MON system, ZIF-7-NH_2 was inspired by the work of Lopez-Cabrelles *et al*., who produced an isoreticular series of iron-based ZIFs incorporating a range of functional groups.[34] However, initial attempts to prepare 100% ZIF-7-NH_2 via the route reported for ZIF-7 resulted in only partial conversion to ZIF-7-NH_2-III during reflux of ZIF-7-NH_2-I in water, resulting in mixed phase material (Figure S7). A mixed ligand system was therefore produced by adding 50 mol% of 5-

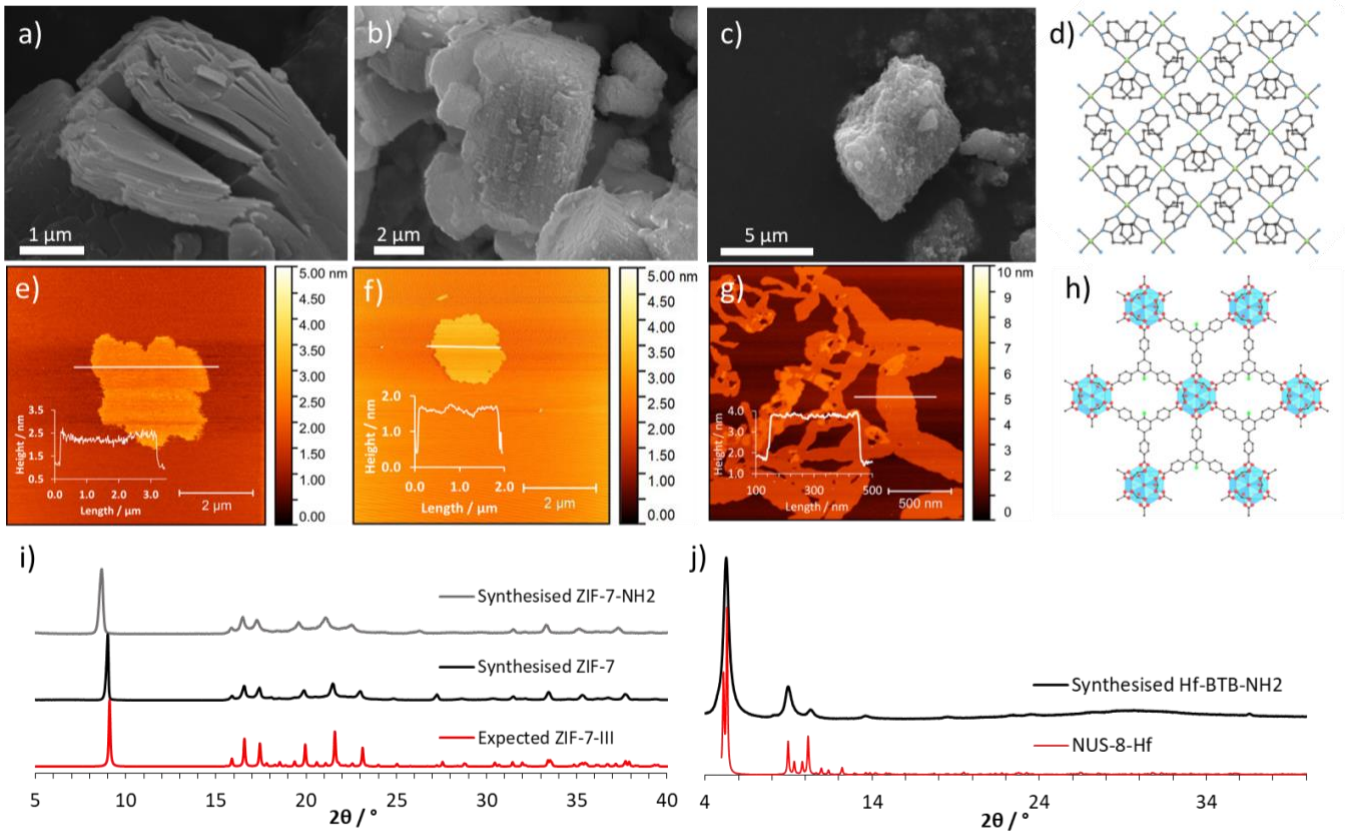

Figure 2: a) Scanning electron microscopy (SEM) image of as-synthesized ZIF-7 layered MOF, b) SEM image of ZIF-7-NH_2 layered MOF, c) SEM image of Hf-BTB-NH_2, d) Schematic of ZIF-7, e) Atomic force microscopy (AFM) image of ZIF-7 nanosheets, f) AFM image of ZIF-7-NH_2 nanosheets, g) AFM image of Hf-BTB-NH_2 nanosheets h) Schematic of Hf-BTB-NH_2, i) expected X-ray powder diffraction (XRPD) pattern of ZIF-7-III (CCDC - 675375) compared to synthesized ZIF-7-III and synthesized ZIF-7-NH_2, j) XRPD pattern of synthesized Hf-BTB-NH_2 compared to NUS-8-Hf.

amino-benzimidazole alongside benzimidazole in the initial step (see section 3.3 in the Supporting Information). The XRPD pattern for the final material matched that reported for ZIF-7-III, confirming successful formation of this novel layered material (Figure 2i). Introducing the amine group produced a small shift in the [002] peak, which is attributed to an increase in the inter-layer distance owing to incorporation of this bulky group (Figure S8). The presence of both ligands within the MOF was confirmed by IR spectroscopy as well as mass spectrometry analysis of the MOF after acid digestion. ^{1}H NMR spectroscopy of the digested material indicated the presence of 20% bim-NH_2: this is consistent with a $Zn_2(bim)_{3.2}(bim\text{-}NH_2)_{0.8}$ composition, as calculated from elemental microanalysis (Figure S5).

ZIF-7-NH_2 nanosheets were accessed in the same way as for ZIF-7. AFM studies indicated mean heights and lengths of 1.6 nm and 400 nm respectively for ZIF-7-NH_2 (Figure 2f and Figure S19). ZIF-7-NH_2 nanosheets had a relatively broad lateral size distribution reaching lengths of 2 µm but the mean height only ranged from 1 to 5 nm. DLS studies indicated a slight increase in the apparent z-average diameter for ZIF-7-NH_2 with a narrower particle size distribution compared to ZIF-7 (Figure S20).

A third MON system was also evaluated. A wide range of nanosheets formed from tricarboxylate linkers connected to Zr_6 or Hf_6 clusters have been reported for use in catalytic,[35–37] and photo- or radio-dynamic therapy applications.[38–41] Here Hf-BTB-NH_2, was prepared by modifying the synthetic protocol reported by Ling *et al.* to introduce Hf_6 metal clusters.[42] Accordingly, hafnium chloride and BTB-NH_2 linker were dissolved in DMF then water and formic acid were added as modulating agents. This mixture was heated for 48 h at 120 °C and the resulting pale viscous colloidal suspension became a homogeneous suspension after washing. Figure 2j shows the XRPD pattern obtained for the Hf-BTB-NH_2 system compared to Hf-BTB (NUS-8) which contains the same key features. The only difference is the introduction of the amine group on the central benzene ring of the BTB linker, see Figure 2h. Further comparison to studies by Ling et al. can be found in Figure S13, which shows a good match to a simulated pattern for Hf_6-BTB MON.[42] The bulk material was then ultrasonicated in water (37 KHz, 12 h) to access nanosheets. The AFM image in Figure 2g shows an example of Hf-BTB-NH_2 nanosheets (average height = 2.7 nm, mean length = 504 nm) with DLS reporting an apparent z-average diameter of 493 nm (Figure S20-S21).

Before phage display was attempted, stability tests were conducted to confirm structural integrity of the MONs under incubation conditions. Each system was exposed to phosphate buffer saline (PBS) for 1 h and 24 h and any structural integrity was determined via XRPD. After incubation for 1 h, the XRPD pattern remained unchanged for each system. After 24 h, only small changes were observed for the ZIFs and no change for Hf-BTB-NH_2 (Figure S23-S25). Moreover, AFM studies revealed no significant change in particle size after incubation (Figure S26).

Selection of Peptide-Functionalized Bacteriophage with High-Affinity MON Binding. Biopanning studies against the three different MON systems were undertaken using genetically modified M13 bacteriophage hosts with a mean length of 880 nm and a mean height of 6.6 nm incorporating a pentavalent display of identical peptides (Figure 1).[43,44] The library of phage- displaying peptides was added to the MONs and incubated for 1 h. Subsequently, a washing step removed any unbound phage, leaving only phage bound to the MONs.

The pH of the system was adjusted to enable bound phage elution, which were then amplified through the infection of *E. coli*. This protocol constituted one panning round. This process was repeated twice by adding the amplified phage from the previous panning round to create increasingly competitive binding conditions and hence identify peptides with the highest affinities. After the third panning round, twelve phage clones were isolated in each case and their DNA was sequenced to determine those peptide sequences that bound with the highest affinity to each MON system.

The identified peptide sequences are shown in Table 1. Only one dominant peptide sequence was isolated for each MON system after three panning rounds, suggesting high selectivity towards that specific peptide. In contrast, Fan et. al. reported 2-3 high affinity binding peptides after the final panning round when using phage display against MOFs.[27] One possible explanation for this difference is that the ultrathin nature of the 2D-MONs means there is essentially just one type of surface available for binding, whereas 3D-MOFs offer multiple faceted surfaces.

Discussion of peptide binding trends. To gain further insight regarding the selection of each preferred peptide sequence, the surface properties of the MONs were compared with those of the consensus peptide. Based on related studies,[21] we hypothesized that three different factors could be important for binding: 1) electrostatic interactions, 2) hydrophobic interactions, 3) specific R-group interactions (Figure 3). Experimental and calculated data to test the relative importance of each type of interaction are presented in Table 1.

To investigate the importance of electrostatic interactions, aqueous electrophoresis studies of the nanosheets were undertaken in the presence and absence of each peptide. Zeta potentials of the three nanosheet systems were determined in dilute PBS (1.37 mmol with respect to NaCl) at 20 ℃ to replicate phage display conditions as closely as possible while meeting instrumental requirements. ZIF-7 and Hf-BTB-NH_2 nanosheets exhibited moderately negative zeta potentials of –30.1 mV and –36.9 mV, respectively. Thus the surface chemistry of the ZIF systems is dominated by the anionic imidazole ligands, rather than the zinc cations. The negative zeta potential for Hf-BTB-NH_2 most likely indicates the presence of surface hydroxyl and phosphate groups, which would confer overall anionic charge. The weakly positive zeta potential observed for ZIF-7-NH_2 is attributed to the presence of surface amine groups. Such a low zeta potential is often associated with an unstable colloidal suspension. However, no sedimentation was observed over the timescale of the experiment and the zeta potential data proved to be reproducible.

Table 1: Summary of the dominant binding peptides identified by phage display for each MON system.

MON System	MON Zeta Potential / mV	MON Contact Angle / °	Peptide Binding Sequence (N'-C'amidated)	Peptide Binding Sequence (N'-C'amidated)	Peptide Isoelectric Point / pH	Predicted overall charge in phage display
ZIF-7	-30.1	149	YNYRNLL	Tyr, Asn, Tyr, Arg, Asn, Leu, Leu	10.15	+2
ZIF-7-NH_2	+2.3	141	NNWWAPA	Asn, Asn, Trp, Trp, Ala, Pro, Ala	14.00	+1
Hf-BTB-NH_2	-36.9	25	FTVRDLS	Phe, Thr, Val, Arg, Asp, Leu, Ser	10.59	+1

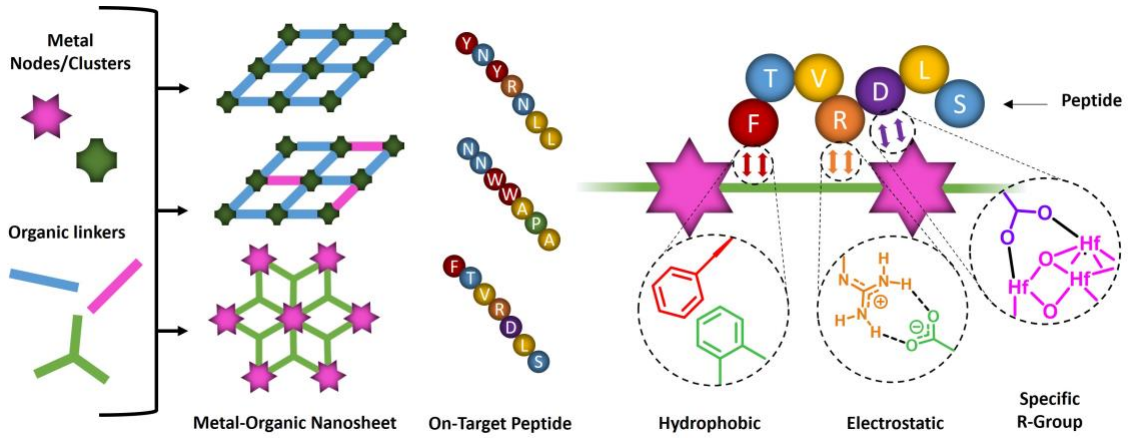

Figure 3: Simplified schematic to show the variety of components used to synthesize three different MON systems where different on-target binding peptides were identified using phage display and examples of the likely hydrophobic, electrostatic and specific R-group affinity interactions.

Table 2: Summary of the binding peptides identified by phage display in panning round 1 and 3 against Hf-BTB-NH_2 with similarities highlighted in yellow.

MON System	Panning round	Peptide Binding Sequence (N'-C'amidated)	Peptide Isoelectric Point / pH	Predicted overall charge in phage display
Hf-BTB-NH_2	3	FTVRDLS	10.59	+1
	1	FTVRDLS	10.59	+1
	1	FPVRDLS	10.59	+1
	1	STVRDFS	10.57	+1
	1	SPVRDNW	10.57	+1
	1	YPERDLC	6.19	-0.1
	1	ISPHPGS	14.00	+1.1

Amino acid side-chain and *N*-terminus pK_a values were used to calculate the isoelectric point of the binding peptide and to predict the overall charge under phage display (PD) conditions (see section 5.3 in the Supporting Information). All three peptides contain a free terminal amine, which should be protonated under PD conditions and hence contribute a +1 charge. The ZIF-7-NH_2 sequence contained no ionizable R-groups; both ZIF-7 and Hf-BTB-NH_2 contained arginine, which confers an additional +1 charge. However, this results in charge balance in the case of Hf-BTB-NH_2 owing to its ionizable aspartic acid residue. The change in zeta potential (ΔZP) was determined upon MON incubation with excess binding peptide (Figure S30). A large ΔZP is observed for ZIF-7 (+56.2 mV) and Hf-BTB-NH_2 (+40.0 mV) but a rather smaller difference is observed for ZIF-7-NH_2 (+20.9 mV). Thus, electrostatic interactions seem to be important for the binding of cationic peptides to the anionic surfaces of ZIF-7 and Hf-BTB-NH_2, but this effect is less significant for peptide binding to ZIF-7-NH_2. As the guanidinium moiety within arginine is most likely charged under the experimental conditions, we infer that it contributes to the overall electrostatic interactions. The importance of arginine interactions with aromatic residues is well-documented in the biomolecular recognition literature.[45,46]

The hydrophobicity of the MON surfaces was investigated using contact angle measurements using DSA100 and compared to the proportion of hydrophobic/hydrophilic residues within the peptide sequences. Nanosheets were packed onto a glass slide, water drops were added using a micro-syringe and the contact angle was measured using a drop shape analyser image system (Figure S22). Although there are some limitations to this approach owing to surface roughness effects, clear differences were observed between the two types of nanosheets.[47] Hf-BTB-NH_2 nanosheets were considerably more hydrophilic (contact angle = 25 °) compared to the ZIF-7 and ZIF-7-NH_2 nanosheets (contact angles of 149 ° and 141 °, respectively). This correlates with the known properties of these MOF classes: the surface chemistry of Hf-BTB-NH_2 systems is dominated by their $Hf_6(\mu_3\text{-}O)_4(\mu_3\text{-}OH)_4(HCO_2)_6$ clusters,[48] while the Zn^{2+} ions of the ZIF systems are largely shielded by the relatively hydrophobic imidazole rings.[49]

This trend in hydrophobicity is mirrored by the consensus binding peptides. The ZIF-7 binding sequence, YNYRNLL, contains several hydrophobic tyrosine and leucine residues, while the ZIF-7-NH_2 peptide sequence, NNWWAPA, contains multiple hydrophobic tryptophan and alanine residues. Benzimidazole derivatives are known enzyme inhibitors owing to π- π interactions between aromatic residues.[50,51] The presence of aromatic Tyr and Trp residues suggest probable π-π interactions with the electron-rich aromatic benzimidazole ligands of ZIF-7. The two peptides for the ZIF MONs both contain two polar asparagine residues, which may confer stability in aqueous solution. In contrast, the Hf-BTB-NH_2 sequence, FTVRDLS, contains a broader range of amino acids, with only three hydrophobic residues (phenylalanine, valine and leucine) alongside hydrophilic residues such as threonine and serine, as well as anionic aspartic acid and cationic arginine residues. This suggests that hydrophobic binding effects are most likely dominant for the ZIF-7-NH_2 but are much less important for the more polar Hf-BTB-NH_2 nanosheets.

At first sight, the presence of the aspartic acid residue in the consensus peptides for the Hf-BTB-NH_2 nanosheets appears to be counter-intuitive given the overall anionic surface character of this MON. However, Lan *et al.* demonstrated that various amino acids can bind to the surface of closely-related Hf_{12}-cluster nanosheets via ligand exchange.[52] In principle, the anionic carboxylate form of aspartic acid (which has a side-chain pK_a of 3.90) may similarly displace the capping formate ligand (pK_a 3.75) to bind to the Hf clusters.

To further explore these trends, strongly binding peptides from the first panning round of Hf-BTB-NH_2 were sequenced (see Table 2). Interestingly, the sequence VRD was conserved in four of the six most strongly binding cases, with RDL conserved in three out of six cases. The conserved nature of this sequence indicates that multiple amino acids are involved in cooperative binding interactions, rather than individual amino acids acting in isolation. Furthermore, the combination of an anionic carboxylate group adjacent to a cationic arginine group and a hydrophobic valine/leucine group appears to be important for effective binding of the consensus peptide sequence.

For the sixth sequence, ISPHPGS, only the final serine is conserved compared to the consensus peptide. In this case, arginine is replaced by a cationic histidine residue in the central fourth position, with the latter flanked by hydrophobic proline residues but no residues with co-ordinating carboxylate R-groups. The constrained proline rings means that this peptide is likely to have a significantly different set of interactions with the MON surface. Presumably, this produces a local minimum on the energy binding landscape.

MON-coated QCM sensors for the detection of bacteriophage- displaying peptides. Over the past decade, various quartz crystal microbalance (QCM) based biosensors have been developed that offer high sensitivity and short detection times.[53–57] A typical QCM biosensor contains either a

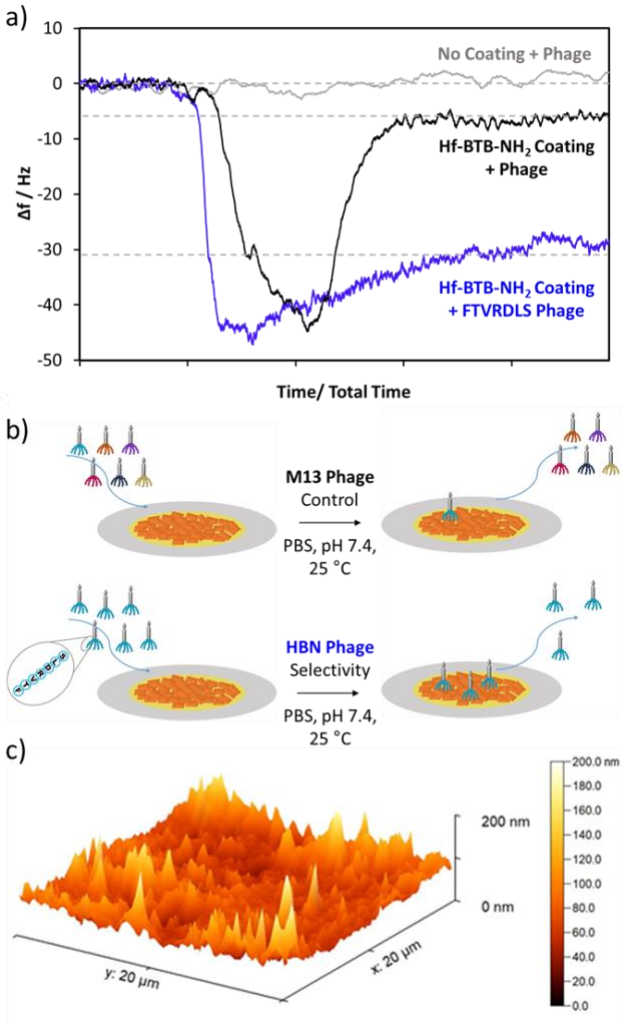

Figure 4: a) Change in frequency, Δ*f*, observed for a silica QCM sensor with no coating (grey) and a ~100 nm Hf-BTB-NH_2 coating after exposure to an aqueous solution of M13 phage in PBS at pH 7.4. Δ*f* was also determined for a ~100 nm Hf-BTB-NH_2-coated silica QCM sensor after exposure to a FTVRDLS-functionalized phage in PBS at pH 7.4, b) Schematic illustration of the difference between exposing this Hf-BTB-NH_2-coated QCM sensor to phage and FTVRDLS phage, c) AFM image of the Hf-BTB-NH_2 coated silica QCM used to determine the mean coating thickness of ~100 nm.

natural or synthetic biomolecular recognition components such as antibodies or molecularly-imprinted polymers (MIPs) coated on a QCM surface. Natural receptors suffer from instability while technical issues associated with MIPs lead to sub-optimal detection limits.[55] We hypothesized that 2D-MONs might offer an alternative biomolecular recognition platform because they constitute a highly stable periodic array of active sites and can be easily processed to form thin films. Examples of 3D-MOF based QCM sensors for vapor/gas detection have been reported but such coatings are relatively thick (~ 1 μm).[58,59] A 2D-MON based QCM sensor has been produced for ammonia detection but as far as we are aware there have been no other studies involving MON-based QCM sensors.[60] QCM was used to assess intrinsic structural changes within MON-based water filtration membranes but not utilized as a sensor.[61] Xie *et al.* designed a covalent-organic framework nanosheet-based QCM sensor to detect miRNA but in this case the nanosheet was simply employed to enhance signal generation in a complex probe DNA system.[62]

One major advantage of a QCM sensor is its sensitivity: detectable changes in adsorbed mass are of the order of one nanogram per cm^2. The simplest model relating Δ*f* to *m* is the Sauerbrey equation,[63] which is used to calculate the mass of the adsorbate.

Silica-based QCM substrates were coated with MONs to investigate their performance in sensing various viruses at a constant flow rate of 0.018 ml min^{-1}. The Hf-BTB-NH_2 system was selected as it was the most stable in PBS (Figure S25) and minimal signal drift was observed. This QCM sensor had a Hf-BTB-NH_2 coating of mean thickness of approximately 100 nm, see Figure 4c. Phage-displaying FTVRDLS, the consensus peptide for Hf-BTB-NH_2, was compared with generic 7-mer peptides as a control to assess the extent of non-specific binding.

QCM data obtained using a sensor with no MON coating (grey) and two sensors coated with Hf-BTB-NH_2 MON (black and blue) are shown in Figure 4. Uncoated and MON-coated QCM sensors were exposed to control phage (grey and black). The uncoated QCM sensor showed no Δ*f* and the MON-coated sensor with generic phage exhibited only a small Δ*f*, which corresponds to an adsorbed amount of just 0.38 $mg{\cdot}m^{-2}$. These observations indicate a weak interaction between the MON surface and the generic phage but no detectable interaction with the uncoated silica sensor control. In contrast, the selective phage (displaying FTVRDLS) exhibited a much greater Δ*f* corresponding to an adsorbed amount of 1.87 $mg{\cdot}m^{-2}$; a 5-fold increase from the control phage. This confirms that phage display identified a selective peptide and that MON-based QCM sensors can be readily constructed.

Binding performance of peptides to synthesised Hf-BTB-NH_2 nanosheets. QCM studies provided strong evidence of highly selective binding to the phage. However, investigations of individual peptides were unsuccessful owing to the relatively high flow rates required for the set-up. To gain a better understanding of the recognition capabilities of the nanosheets for isolated peptides not attached to phage, zeta potential and surface plasmon resonance (SPR) measurements were undertaken to determine the dissociation constant (K_d) and equilibrium dissociation constant (K_D) for the on-target and off-target peptides to Hf-BTB-NH_2.

A saturation binding experiment was conducted in which zeta potential measurements were recorded for a stock MON solution (1 mg/ml in 1.37 mmol PBS w.r.t. NaCl) incubated with various peptide concentrations (Figure S32). The K_d for FTVRDLS binding to Hf-BTB-NH_2 was calculated to be 74 ± 22 μM. Off-target binding studies of YNYRNLL and NNWWAPA against Hf-BTB-NH_2 were also conducted, with the K_d determined to be 285 ± 23 μM and 1393 ± 200 μM respectively. This corresponds to an approximate 4-fold and 19-fold increase in the dissociation constant relative to the on-target binding of FTVRDLS. This is consistent with the phage display identified 12-mer peptide binding studies against MOFs reported by Fan et. al., who found all values lying within the micromolar range.[27] The smaller difference in K_d for YNYRNLL most likely reflects similarities between these arginine-bearing peptides, which leads to strong binding to the anionic MON surfaces. Hence Hf-BTB-NH_2 shows a high degree of selectivity for the consensus peptide identified

Table 3: Calculated equilibrium dissociation constant (K_D) of imprinted materials. All experiments performed under ambient conditions. n=3.

	K_D (M)
Target Peptide - FTVRDLS	4.15×10^{-10} ($\pm 0.32 \times 10^{-10}$)
Off-target Peptide - YNYRNLL	2.71×10^{-7} ($\pm 0.48 \times 10^{-7}$)
Off-target Peptide - NNWWAPA	1.91×10^{-6} ($\pm 0.27 \times 10^{-6}$)

through the biopanning studies, which makes it a promising candidate for use as a sensitive peptide recognition surface.

SPR analysis was used to determine the overall equilibrium dissociation constant (K_D) of Hf-BTB-NH_2 nanosheets towards these peptides and the data is summarized in Table 3. The dried nanosheets were suspended in 1 mL of the running buffer (PBS pH 7.4 and 0.01 % Tween 20), with the addition of sodium acetate for SPR analysis. A planar polyethylene glycol/carboxyl coated Au chip was activated using NHS and EDC, followed by the addition of the nanosheet dispersion. Finally, a quenching solution of ethanolamine was used to deactivate any unreacted carboxyl groups and wash away any unbound nanosheets.

The SPR sensorgrams (Figure S31) show the interactions of the target peptide FTVRDLS at five different concentrations with the Hf-BTB-NH_2 nanosheets (Figure S31A). To study cross-reactivity and non-specific binding to the nanosheets were also investigated with non-target peptides YNYRNLL (Figure S31B) and NNWWAPA (Figure S31C) were also examined, Tween 20 surfactant (0.01%) was added to the running buffer to minimize non-specific binding. Experiments were repeated in triplicate and the SPR curves were fitted to a 1:1 interaction model.

The K_D value of the interaction between target peptide FTVRDLS and the nanosheet has been calculated at 0.415 nM (Table 3). This shows that Hf-BTB-NH_2 nanosheets exhibit extremely high affinity towards the target peptide FTVRDLS and the strength of this specific interaction is comparable to natural recognition components.[28] The interaction of this nanosheet with non-target peptides, produced K_D values of 271 nM and 1910 nM for YNYRNLL and NNWWAPA, respectively. This suggests a high degree of selectivity and specificity towards the target peptide, with an approximate 650-fold and 4600-fold improvement in affinity compared with off-target YNYRNLL and NNWWAPA, respectively. This is further evidence that Hf-BTB-NH_2 nanosheets are excellent candidates as biomolecular recognition components within next-generation biosensors.

CONCLUSION

Achieving high selectivity for a specific peptide sequence amongst the myriad of possibilities is a formidable challenge with enormous potential for the development of next-generation biosensors. Here we demonstrate that MONs confer selectivity through multiple weak interactions with peptides. Three ultrathin MON systems were prepared: ZIF-7 and ZIF-7-NH_2 possess similar chemical structures while Hf-BTB-NH_2 differs significantly. PD biopanning was exploited to screen a library of 1×10^{13} possible combinations of 7 amino acids and hence identify the strongest binding peptide sequence for each of the three different MONs. In contrast to previous biopanning studies on MOFs, only a single consensus peptide sequence was identified in each case; this is attributed to the MONs surface comprising only a single facet.

Comparing zeta potential data and contact angle measurements obtained for these MONs with calculated properties for the peptide sequences indicates that a combination of electrostatic, hydrophobic and coordination bonding interactions are important for strong peptide-MON binding. In particular, the VRDL sequence is highly conserved for peptides that bind strongly to Hf-BTB-NH_2. A QCM-MON sensor functionalized with Hf-BTB-NH_2 was constructed as a model for binding and a 5-fold increase in selectivity was demonstrated for phage displaying the consensus peptide compared to phage displaying generic peptides. Furthermore, SPR studies confirmed that the FTVRDLS consensus sequence binds up to 4600 times more strongly to Hf-BTB-NH2 than to the off-target peptide sequences with values comparable to those achieved by antibodies ($K_D = 4 \times 10^{-10}$). Thus we anticipate that the diverse and highly tunable surface chemistry of MONs combined with the rapid sampling of binding peptides provided by phage display will inform the design of exquisitely selective next-generation biomolecular recognition surfaces with extremely high affinity for biomedically relevant peptides.

MATERIALS AND METHODS

Synthesis of ZIF-7 nanosheets. First, ZIF-7-I nanoparticles were prepared by adding DMF (250 mL, 3.25 mol) to $Zn(NO_3)\cdot 6H_2O$ (755 mg, 2.54 mmol) and benzimidazole (1.92 g, 16.28 mmol). This mixture was left at room temperature for 72 h, stirring for the first hour only. The precipitate was then collected by centrifugation (12,000 rpm for 1 h). Particles were purified by thoroughly washing via redispersion in methanol then centrifugation (12,000 rpm for 1 h). This wash-centrifugation cycle was repeated three times before drying at 50 °C for 18 h in a vacuum oven. The particles were further dried at 120 °C for 48 h in a vacuum oven.

ZIF-7-I was redispersed in distilled water (0.5 wt%) and refluxed at 100 °C for 24 h. The turbid mixture was washed with distilled water once and methanol three times by redispersion and centrifuging (12,000 rpm for 1 h). The white solid was then dried at 50 °C overnight to obtain ZIF-7-III. Finally, ZIF-7-III (80 mg) was ultrasonicated in a 1:1 v/v methanol/*n*-propanol mixture (120 mL) at 80 KHz for 2 h to access nanosheets. After centrifugation at 500 rpm for 5 min, the resulting supernatant containing the nanosheets was then centrifuged at 12,000 rpm for 1 h.

Synthesis of ZIF-7-NH_2 nanosheets. First, ZIF-7-NH_2-I nanoparticles were prepared by adding DMF (125 mL, 1.63 mol) to $Zn(NO_3)\cdot 6H_2O$ (755 mg, 2.54 mmol) and

benzimidazole (962 mg, 8.14 mmol) and 5-aminobenzimidazole (1.08 g, 8.11 mmol). This mixture was left at 30 °C for 2 weeks, stirring for the first hour only. ZIF-7-NH_2 nanoparticles were then collected by centrifugation (12,000 rpm for 1 h). Particles were purified by thoroughly washing via redispersion in methanol followed by centrifugation (12,000 rpm for 1 h). This wash-centrifugation cycle was repeated three times before drying at 50 °C for 18 h in a vacuum oven. The particles were further dried at 120 °C for 48 h in a vacuum oven.

ZIF-7-NH_2-I was redispersed in distilled water at a concentration of 0.5 wt % and refluxed at 100 °C for 1 week. The turbid mixture was washed with distilled water once and methanol three times, and then dried at 50 °C overnight to obtain ZIF-7-NH_2-III. 80 mg ZIF-7-NH_2-III was ultrasonicated in 1:1 v/v methanol/*n*-propanol (120 mL) at 80 KHz for 2 h to access nanosheets. After centrifugation at 500 rpm for 5 min, the resulting supernatant containing the nanosheets was then centrifuged at 12,000 rpm for 1 h.

Synthesis of Hf-BTB-NH_2 nanosheets. To prepare Hf-BTB-NH_2 MONs, $HfCl_4$ (34.59 mg, 0.108 mmol) and 2,4,6-tris(4-carboxyphenyl)aniline (32.87 mg, 0.072 mmol) were added to a 20 mL screw-cap glass vial. DMF (12.5 mL) was added and the mixture was dissolved with the aid of ultrasonics to obtain a clear solution. Formic acid (2.5 mL) and H_2O (0.7 mL) were added, then the vial was sealed and placed in a 120 °C oven for 48 h. The vial was taken out of the oven and cooled to room temperature. The turbid solution was centrifuged to collect Hf-BTB-NH_2 as a pale-yellow precipitate. The precipitate was washed multiple times with DMF, followed by ethanol. To prevent stacking of the MON layers, Hf-BTB-NH_2 was stored in ethanol until needed for further studies.

Phage Display. MON binding peptides were isolated from a random 7-mer peptide library (New England Biolabs, Inc.) using the phage display protocol. The DNA sequences of the 7-mer peptides from the combinatorial peptide library are fused to the gIII of the bacteriophage M13. The peptides are separated from the pIII major coat protein by a short spacer sequence (GGGS). The peptide library has complexities on the order of 10^{13} independent clones, which is sufficient to encode the 1.28 x 10^9 possible 7-mer peptide sequences. General phage methods were conducted according to the manufacturer's recommendations.

MONs were incubated with the phage library in 2x blocking buffer (BB) phosphate buffered saline for 1 h on a rotating blood wheel. The particles were washed three times with PBS to remove unbound phage. After each wash, the frameworks were isolated by centrifugation (relative centrifugal force (RCF) 10 000 × g) for 10 min, and the supernatant was discarded. Bound phage were eluted with 0.2 M glycine pH 2.2, followed by trimethylamine. This resulted in MON digestion for ZIF-7 and ZIF-7-NH_2 so it is assumed that all bound phage were eluted. The eluted phage were amplified in E. coli (ER2738) and purified by poly(ethylene glycol)-8000/sodium chloride (PEG/NaCl) precipitation with subsequent centrifugation steps. In subsequent biopanning rounds, at least 5×10^{10} phage were applied to a fresh solution of MONs in PBS. A total of three panning rounds were conducted to enrich the peptide pool with the highest affinity binders. For each MON system, 12 phage clones were analyzed by DNA sequencing.

Peptide binding study – zeta potential. Hf-BTB-NH_2 solution (1 mg/ml) in diluted PBS (1.37 mmol wrt. NaCl) was incubated for 1 h with various concentrations of the three identified binding peptides. Zeta potentials were determined after 1 h of incubation to examine any change in this parameter for the various peptides. The equation for K_d is provided in section 4.1 of the Supporting Information.

Immobilisation of nanosheets onto the SPR Sensor Surface. Planar polyethylene glycol/carboxyl coated Au chips, purchased from Reichert Technologies (Buffalo, USA) were installed onto a Reichert 2 SPR following the manufacturer's instructions. The sensor surface was then preconditioned by running buffer PBST (PBS pH 7.4 and 0.01 % Tween 20) at 10 µL min^{-1} until a stable baseline was obtained. The flow rate of 10 µL was maintained throughout the immobilisation process. In order to activate carboxyl groups on the surface of the sensor chip, a freshly prepared aqueous solution (1 mL) of EDC (40 mg) and NHS (10 mg) was injected onto the sensor chip surface for 6 minutes. To the activated surface, 300 µg of the Hf-BTB-NH_2 nanosheets dissolved in 1 mL of the running buffer (PBST) and 10 mM sodium acetate, was injected only to the left channel of the surface for 1 minute. Finally, quenching solution (1 M ethanolamine, pH 8.5) was injected for 8 minutes to deactivate carboxyl groups and wash away the unbound Hf-BTB-NH_2 nanosheets. A continuous flow of running buffer (PBST) at 10 µL min^{-1} was maintained after Hf-BTB-NH_2 nanosheet immobilisation. SPR assays were carried out after a stable baseline was achieved. The left channel was the working channel, and the right channel was the reference.

Kinetic Analysis Using SPR. Kinetic analysis was initiated by injection of the running buffer PBST (blank) onto the Hf-BTB-NH_2 immobilised sensor surface for 2 minutes, followed by PBST for 5 minutes. The binding kinetics of an individual Hf-BTB-NH_2 nanosheet to the selected target was determined from serial dilutions (five concentrations, 4-64 nM) of the selected target under study. Each dilution was injected for 2 minutes (association) followed by PBST for 5 minutes (dissociation). After dissociation, the target was removed from the immobilized surface by injecting regeneration buffer (10 mM Glycine-HCl, pH 2) for 1 minutes followed by PBST for 1 minutes. The same procedures were repeated for the remaining four dilutions of the target. After the analyses were completed, signals from the left channel were subtracted from signals from their respective reference channel (the right channel).

The SPR responses from five concentrations of the target compound (4-64 nM) were fitted to a 1:1 bio-interaction (BI) mdel (Langmuir fit model) utilizing TraceDrawer software. Association rate constants (ka), dissociation rate constants (kd), and maximum binding (Bmax) were fitted globally, whereas the BI signal was fitted locally. The equilibrium dissociation constant (K_D) was calculated from the ratio kd/ka.

Preparation of MON-based QCM sensors. Quartz crystal microbalance (QCM) sensors coated with a 50 nm silica overlayer (QSX 303, ~5 MHz fundamental frequency) were purchased from Q-Sense (Sweden). Each sensor was cleaned according to the manufacturer's instructions. This protocol involved (i) UV/O_3 treatment for 15 min (Bioforce UV/O_3 cleaner, ~9 mW cm^{-2}, λ = 254 nm), (ii) exposure to 2% w/w sodium dodecylsulfate solution for 30 min, (iii) copious rinsing with deionized water and drying under N_2, (iv) a final UV/O_3 treatment for 15 min.

The sensor was prepared by adding 10 x 10 µL of MON solution (1 mg/ml, ethanol) dropwise to the clean QCM substrate while spin coating at 3,000 rpm for 10 min. The thickness of the resulting MON coating was measured using AFM to be approximately 100 nm.

QCM measurements were performed using an openQCM NEXT instrument (Novatech Srl., Italy) equipped with a temperature-controlled cell connected to a Masterflex Digital Miniflex peristaltic pump (Cole-Parmer Instrument Company, UK). All experiments were conducted in PBS buffer (pH 7.4) and no measurements were undertaken until the sensor frequency exhibited a drift of less than 0.1 Hz min^{-1}; this typically occurred within 1 h of filling the cell. Once a stable signal was obtained, the phage solutions (1 x 10^{12} PFU / mL) in PBS were passed through the cell at a constant flow rate of 0.018 mL min^{-1} (minimum flow volume = 0.20 mL).

The adsorbed amount can be calculated using various models.[64–66] The simplest and most widely applied of these is based on the Sauerbrey equation, which relates the change in frequency, Δf, directly to the change in adsorbed mass per unit area, m,

$$m = C \times \frac{\Delta f}{n}$$

where C is a sensitivity constant (-0.177 (mg·m^{-2}) × Hz^{-1}), Δf is the change in the resonant frequency (Hz), and n is the overtone number. The third harmonic (n = 3) was used to calculate the adsorbed amount to avoid experimental artifacts associated with the fundamental harmonic that may occur if the sample is imperfectly mounted on the sensor.[66–68]

ASSOCIATED CONTENT

Supporting Information. Materials synthesis and characterization, XRPD, ATR-IR, SEM, TGA, Tyndall scattering images, AFM, DLS, zeta potential data, contact angle images, binding study data and calculations.

AUTHOR INFORMATION

Corresponding Author

* E-mail: jona.foster@sheffield.ac.uk

Funding Sources

EPSRC (EP/T012455/1)

ACKNOWLEDGMENTS

The authors acknowledge the EPSRC for funding (EP/S021124/1). ACW undertook the synthesis and characterisation of the ZIF-7 based MONs, biopanning and peptide binding studies and MON-QCM sensors as well as analysing the data and drafting the manuscript. ECJ provided training on QCM and added data discussion and editing of the manuscript. RRRP synthesised the Hf-BTB-NH2 MONs and edited the manuscript. MVS undertook SPR experiments and aided data analysis. NWT aided data discussion and editing of the manuscript. SPA provided the QCM equipment and edited the manuscript. SSS co-supervised the project and edited the manuscript. JAF supervised the project, aided with data discussion and drafting and editing of the manuscript. We also thank Michael Harris, Jiangtian Tan, Chris Hill and the University of Sheffield BioMedical Sciences EM unit for SEM analysis. Dr. Raffaele Battaglia and Marco Mauro at Novaetech S.r.l. (Pompeii, Italy) are thanked for their excellent technical support regarding the QCM studies.

ABBREVIATIONS

2D-MON, two-dimensional metal-organic nanosheet; 3D-MOF, three-dimensional metal-organic framework; bim, benzimidazole; bim-NH_2, 5-aminobenzimidazole; BTB-NH_2, 2,4,6-tris(4-carboxyphenyl)aniline; C, sensitivity constant; K_d, equilibrium dissociation constant; m, mass; MIPS, molecularly imprinted polymers; MOF, metal-organic framework; n, overtone number; MON, metal-organic nanosheet; PBS, phosphate buffered saline; QCM, quartz crystal microbalance; ZIF, zeolitic imidazolate framework. SPR, Surface Plasmon Resonance

REFERENCES

(1) Kahn, K.; Plaxco, K. W. Principles of Biomolecular Recognition. In *Recognition Receptors in Biosensors*; Springer New York: New York, NY, 2010; 3–45. https://doi.org/10.1007/978-1-4419-0919-0_1.

(2) Rohaizad, N.; Mayorga-Martinez, C. C.; Fojtů, M.; Latiff, N. M.; Pumera, M. Two-Dimensional Materials in Biomedical, Biosensing and Sensing Applications. *Chemical Society Reviews*. 2021, 619–657. https://doi.org/10.1039/d0cs00150c.

(3) Huang, H.; Feng, W.; Chen, Y. Two-Dimensional Biomaterials: Material Science, Biological Effect and Biomedical Engineering Applications. *Chemical Society Reviews*. 2021, 11381–11485. https://doi.org/10.1039/d0cs01138j.

(4) Bolotsky, A.; Butler, D.; Dong, C.; Gerace, K.; Glavin, N. R.; Muratore, C.; Robinson, J. A.; Ebrahimi, A. Two-Dimensional Materials in Biosensing and Healthcare: From in Vitro Diagnostics to Optogenetics and Beyond. *ACS Nano* **2019**, *13*, 9781–9810. https://doi.org/10.1021/acsnano.9b03632.

(5) Murali, A.; Lokhande, G.; Deo, K. A.; Brokesh, A.; Gaharwar, A. K. Emerging 2D Nanomaterials for Biomedical Applications. *Materials Today*. 2021, 276–302. https://doi.org/10.1016/j.mattod.2021.04.020.

(6) Su, S.; Sun, Q.; Gu, X.; Xu, Y.; Shen, J.; Zhu, D.; Chao, J.; Fan, C.; Wang, L. Two-Dimensional Nanomaterials for Biosensing Applications. *TrAC - Trends Anal. Chem.* **2019**, *119*, 115610. https://doi.org/10.1016/j.trac.2019.07.021.

(7) Cun, J.-E.; Fan, X.; Pan, Q.; Gao, W.; Luo, K.; He, B.; Pu, Y. Copper-Based Metal–Organic Frameworks for Biomedical Applications. *Adv. Colloid Interface Sci.* **2022**, *305*, 102686. https://doi.org/10.1016/j.cis.2022.102686.

(8) Arun Kumar, S.; Balasubramaniam, B.; Bhunia, S.; Jaiswal, M. K.; Verma, K.; Prateek; Khademhosseini, A.; Gupta, R. K.; Gaharwar, A. K. Two-dimensional Metal Organic Frameworks for Biomedical Applications. *WIREs Nanomedicine and Nanobiotechnology* **2021**, *13*, e1674. https://doi.org/10.1002/wnan.1674.

(9) Nicks, J.; Sasitharan, K.; Prasad, R. R. R.; Ashworth, D. J.; Foster, J. A. Metal–Organic Framework Nanosheets: Programmable 2D Materials for Catalysis, Sensing, Electronics, and Separation Applications. *Adv. Funct. Mater.* **2021**, *31*, 2103723. https://doi.org/10.1002/adfm.202103723.

(10) Zhao, D.; Zhang, W.; Wu, Z. H.; Xu, H. Nanoscale Metal−Organic Frameworks and Their Nanomedicine Applications. *Frontiers in Chemistry*. Frontiers Media S.A. January 24, 2022, 1243. https://doi.org/10.3389/fchem.2021.834171.

(11) Zhao, M.; Wang, Y.; Ma, Q.; Huang, Y.; Zhang, X.; Ping, J.; Zhang, Z.; Lu, Q.; Yu, Y.; Xu, H.; Zhao, Y.; Zhang, H. Ultrathin 2D Metal-Organic Framework Nanosheets. *Adv. Mater.* **2015**, *27*, 7372–7378. https://doi.org/10.1002/adma.201503648.

(12) Zhang, H.; Luo, B.; An, P.; Zhan, X.; Lan, F.; Wu, Y. Interaction of Nucleic Acids with Metal-Organic Framework Nanosheets by Fluorescence Spectroscopy and Molecular Dynamics Simulations. *ACS Appl. Bio Mater.* **2022**, *5*, 3500–3508. https://doi.org/10.1021/acsabm.2c00431.

(13) Yang, Y.; Hu, G. B.; Liang, W. Bin; Yao, L. Y.; Huang, W.; Zhang, Y. J.; Zhang, J. L.; Wang, J. M.; Yuan, R.; Xiao, D. R. An AIEgen-Based 2D Ultrathin Metal-Organic Layer as an Electrochemiluminescence Platform for Ultrasensitive Biosensing of Carcinoembryonic Antigen. *Nanoscale* **2020**, *12*, 5932–5941. https://doi.org/10.1039/c9nr10712f.

(14) Yan, M.; Ye, J.; Zhu, Q.; Zhu, L.; Huang, J.; Yang, X. Ultrasensitive Immunosensor for Cardiac Troponin i Detection Based on the Electrochemiluminescence of 2D Ru-MOF Nanosheets. *Anal. Chem.* **2019**, *91*, 10156–10163. https://doi.org/10.1021/acs.analchem.9b02169.

(15) Lin, Y.; Sun, Y.; Dai, Y.; Sun, W.; Zhu, X.; Liu, H.; Han, R.; Gao, D.; Luo, C.; Wang, X. A "Signal-on" Chemiluminescence Biosensor for Thrombin Detection Based on DNA Functionalized Magnetic Sodium Alginate Hydrogel and Metalloporphyrinic Metal-Organic Framework Nanosheets. *Talanta* **2020**, *207*, 120300. https://doi.org/10.1016/j.talanta.2019.120300.

(16) Zeng, Y.; Wang, M.; Sun, Z.; Sha, L.; Yang, J.; Li, G. Colorimetric Immunosensor Constructed Using 2D Metal–Organic Framework Nanosheets as Enzyme Mimics for the Detection of Protein Biomarkers. *J. Mater. Chem. B* **2022**, *10*, 450–455. https://doi.org/10.1039/d1tb02192c.

(17) de Azambuja, F.; Loosen, A.; Dragan, C.; van den Besselaar, M.; Harvey, J. N.; Parac-Vogt, T. N. En Route to a Heterogeneous Catalytic Direct Peptide Bond Formation by Zr-Based Metal-Organic Framework Catalysts. *ACS Catal.* **2021**, *11*, 7647–7658. https://doi.org/10.1021/acscatal.1c01782.

(18) Loosen, A.; De Azambuja, F.; Smolders, S.; Moons, J.; Simms, C.; De Vos, D.; Parac-Vogt, T. N. Interplay between Structural Parameters and Reactivity of Zr6-Based MOFs as Artificial Proteases. *Chem. Sci.* **2020**, *11*, 6662–6669. https://doi.org/10.1039/d0sc02136a.

(19) Giang, H.; Ly, T.; Fu, G.; Kondinski, A.; Bueken, B.; De Vos, D.; Parac-Vogt, T. N. Superactivity of MOF-808 toward Peptide Bond Hydrolysis. *J. Am. Chem. Soc* **2018**, *140*, 2023. https://doi.org/10.1021/jacs.8b01902.

(20) Ly, H. G. T.; Fu, G.; De Azambuja, F.; De Vos, D.; Parac-Vogt, T. N. Nanozymatic Activity of UiO-66 Metal-Organic Frameworks: Tuning the Nanopore Environment Enhances Hydrolytic Activity toward Peptide Bonds. *ACS Appl. Nano Mater.* **2020**, *3*, 8931–8938. https://doi.org/10.1021/acsanm.0c01688.

(21) Loosen, A.; de Azambuja, F.; Parac-Vogt, T. N. Which Factors Govern the Adsorption of Peptides to Zr(Iv)-Based Metal–Organic Frameworks? *Mater. Adv.* **2022**, *3*, 2475–2487. https://doi.org/10.1039/d1ma01027a.

(22) Smith, G. P.; Petrenko, V. A. Phage Display. *Chem. Rev.* **1997**, *97*, 391–410. https://doi.org/10.1021/cr960065d.

(23) Rawlings, A. E.; Bramble, J. P.; Tang, A. A. S.; Somner, L. A.; Monnington, A. E.; Cooke, D. J.; McPherson, M. J.; Tomlinson, D. C.; Staniland, S. S. Phage Display Selected Magnetite Interacting Adhirons for Shape Controlled Nanoparticle Synthesis. *Chem. Sci.* **2015**, *6*, 5586–5594. https://doi.org/10.1039/c5sc01472g.

(24) Li, C.; Liu, J.; Shaozhou, W.; Bai, X.; Zhang, Q.; Hua, R.; Liu, J.-H.; Liu, M.; Zhang, Y. Epitope Identification and Application for Diagnosis of Duck Tembusu Virus Infections in Ducks. *Viruses* **2016**, *8*, 306. https://doi.org/10.3390/v8110306.

(25) Kouzmitcheva, G. A.; Petrenko, V. A.; Smith, G. P. Identifying Diagnostic Peptides for Lyme Disease through Epitope Discovery. *Clin. Diagnostic Lab. Immunol.* **2001**, *8*, 150–160. https://doi.org/10.1128/CDLI.8.1.150-160.2001.

(26) Reiss, B. D.; Mao, C.; Solis, D. J.; Ryan, K. S.; Thomson, T.; Belcher, A. M. Biological Routes to Metal Alloy Ferromagnetic Nanostructures. *Nano Lett.* **2004**, *4*, 1127–1132. https://doi.org/10.1021/nl049825n.

(27) Fan, G.; Dundas, C. M.; Zhang, C.; Lynd, N. A.; Keitz, B. K. Sequence-Dependent Peptide Surface Functionalization of Metal-Organic Frameworks. *ACS Appl. Mater. Interfaces* **2018**, *10*, 18601–18609. https://doi.org/10.1021/acsami.8b05148.

(28) Landry, J. P.; Ke, Y.; Yu, G. L.; Zhu, X. D. Measuring Affinity Constants of 1450 Monoclonal Antibodies to Peptide Targets with a Microarray-Based Label-Free Assay Platform. *J. Immunol. Methods* **2015**, *417*, 86–96. https://doi.org/10.1016/j.jim.2014.12.011.

(29) Li, Y.; Liang, F.; Bux, H.; Yang, W.; Caro, J. Zeolitic Imidazolate Framework ZIF-7 Based Molecular Sieve Membrane for Hydrogen Separation. *J. Memb. Sci.* **2010**, *354*, 48–54. https://doi.org/10.1016/j.memsci.2010.02.074.

(30) Zhang, S.; Yao, W.; Ying, J.; Zhao, H. Polydopamine-Reinforced Magnetization of Zeolitic Imidazolate Framework ZIF-7 for Magnetic Solid-Phase Extraction of Polycyclic Aromatic Hydrocarbons from the Air-Water Environment. *J. Chromatogr. A* **2016**, *1452*, 18–26. https://doi.org/10.1016/j.chroma.2016.05.039.

(31) Kang, C.-H.; Lin, Y.-F.; Huang, Y.-S.; Tung, K.-L.; Chang, K.-S.; Chen, J.-T.; Hung, W.-S.; Lee, K.-R.; Lai, J.-Y. Synthesis of ZIF-7/Chitosan Mixed-Matrix Membranes with Improved Separation Performance of Water/Ethanol Mixtures. *J. Memb. Sci.* **2013**, *438*, 105–111. https://doi.org/10.1016/j.memsci.2013.03.028.

(32) Liu, H.-L.; Chang, Y.-J.; Fan, T.; Gu, Z.-Y. Two-Dimensional Metal–Organic Framework Nanosheets as a Matrix for Laser Desorption/Ionization of Small Molecules and Monitoring Enzymatic Reactions at High Salt Concentrations. *Chem. Commun.* **2016**, *52*, 12984–12987. https://doi.org/10.1039/C6CC07371A.

(33) Peng, Y.; Li, Y.; Ban, Y.; Jin, H.; Jiao, W.; Liu, X.; Yang, W. Metal-Organic Framework Nanosheets as Building Blocks for Molecular Sieving Membranes. *Science (80-.).* **2014**, *346*, 1356–1359. https://doi.org/10.1126/science.1254227.

(34) López-Cabrelles, J.; Mañas-Valero, S.; Vitórica-Yrezábal, I. J.; Bereciartua, P. J.; Rodríguez-Velamazán, J. A.; Waerenborgh, J. C.; Vieira, B. J. C.; Davidovikj, D.; Steeneken, P. G.; van der Zant, H. S. J.; Mínguez Espallargas, G.; Coronado, E. Isoreticular Two-Dimensional Magnetic Coordination Polymers Prepared through Pre-Synthetic Ligand Functionalization. *Nat. Chem.* **2018**, *10*, 1001–1007. https://doi.org/10.1038/s41557-018-0113-9.

(35) Zhao, J.; Chen, R.; Huang, J.; Wang, F.; Tao, C.-A.; Wang, J. Facile Synthesis of Metal–Organic Layers with High Catalytic Performance toward Detoxification of a Chemical Warfare Agent Simulant. *ACS Appl. Mater. Interfaces* **2021**, *13*, 40863–40871. https://doi.org/10.1021/acsami.1c08365.

(36) Quan, Y.; Lan, G.; Shi, W.; Xu, Z.; Fan, Y.; You, E.; Jiang, X.; Wang, C.; Lin, W. Metal–Organic Layers Hierarchically Integrate Three Synergistic Active Sites for Tandem Catalysis.

Angew. Chemie Int. Ed. **2021**, *60*, 3115–3120. https://doi.org/10.1002/anie.202011519.

(37) Guo, Y.; Shi, W.; Yang, H.; He, Q.; Zeng, Z.; Ye, J.; He, X.; Huang, R.; Wang, C.; Lin, W. Cooperative Stabilization of the [Pyridinium-CO 2 -Co] Adduct on a Metal–Organic Layer Enhances Electrocatalytic CO 2 Reduction. *J. Am. Chem. Soc.* **2019**, *141*, 17875–17883. https://doi.org/10.1021/jacs.9b09227.

(38) Luo, T.; Fan, Y.; Mao, J.; Yuan, E.; You, E.; Xu, Z.; Lin, W. Dimensional Reduction Enhances Photodynamic Therapy of Metal–Organic Nanophotosensitizers. *J. Am. Chem. Soc.* **2022**, *144*, 5241–5246. https://doi.org/10.1021/jacs.2c00384.

(39) Lan, G.; Ni, K.; Xu, R.; Lu, K.; Lin, Z.; Chan, C.; Lin, W. Nanoscale Metal-Organic Layers for Deeply Penetrating X-Ray-Induced Photodynamic Therapy. *Angew. Chemie* **2017**, *129*, 12270–12274. https://doi.org/10.1002/ange.201704828.

(40) Nash, G. T.; Luo, T.; Lan, G.; Ni, K.; Kaufmann, M.; Lin, W. Nanoscale Metal–Organic Layer Isolates Phthalocyanines for Efficient Mitochondria-Targeted Photodynamic Therapy. *J. Am. Chem. Soc.* **2021**, *143*, 2194–2199. https://doi.org/10.1021/jacs.0c12330.

(41) Lan, G.; Ni, K.; Veroneau, S. S.; Song, Y.; Lin, W. Nanoscale Metal–Organic Layers for Radiotherapy–Radiodynamic Therapy. *J. Am. Chem. Soc.* **2018**, *140*, 16971–16975. https://doi.org/10.1021/jacs.8b11593.

(42) Ling, X.; Gong, D.; Shi, W.; Xu, Z.; Han, W.; Lan, G.; Li, Y.; Qin, W.; Lin, W. Nanoscale Metal–Organic Layers Detect Mitochondrial Dysregulation and Chemoresistance via Ratiometric Sensing of Glutathione and PH. *J. Am. Chem. Soc.* **2021**, *143*, 1284–1289. https://doi.org/10.1021/jacs.0c11764.

(43) Hess, G. T.; Cragnolini, J. J.; Popp, M. W.; Allen, M. A.; Dougan, S. K.; Spooner, E.; Ploegh, H. L.; Belcher, A. M.; Guimaraes, C. P. M13 Bacteriophage Display Framework That Allows Sortase-Mediated Modification of Surface-Accessible Phage Proteins. *Bioconjug. Chem.* **2012**, *23*, 1478–1487. https://doi.org/10.1021/bc300130z.

(44) Burton, D. R. Phage Display. *Immunotechnology* **1995**, *1*, 87–94. https://doi.org/10.1016/1380-2933(95)00013-5.

(45) Burley, S. K.; Petsko, G. A. Amino-Aromatic Interactions in Proteins. *FEBS Lett.* **1986**, *203*, 139–143. https://doi.org/10.1016/0014-5793(86)80730-X.

(46) Patwardhan, S. V.; Patwardhan, G.; Perry, C. C. Interactions of Biomolecules with Inorganic Materials: Principles, Applications and Future Prospects. *J. Mater. Chem.* **2007**, *17*, 2875. https://doi.org/10.1039/b704075j.

(47) Jayaramulu, K.; Geyer, F.; Schneemann, A.; Kment, Š.; Otyepka, M.; Zboril, R.; Vollmer, D.; Fischer, R. A. Hydrophobic Metal–Organic Frameworks. *Adv. Mater.* **2019**, *31*, 1900820. https://doi.org/10.1002/adma.201900820.

(48) Pu, Y.; Yang, Z.; Wee, V.; Wu, Z.; Jiang, Z.; Zhao, D. Amino-Functionalized NUS-8 Nanosheets as Fillers in PIM-1 Mixed Matrix Membranes for CO2 Separations. *J. Memb. Sci.* **2022**, *641*, 119912. https://doi.org/10.1016/j.memsci.2021.119912.

(49) Zhao, P.; Lampronti, G. I.; Lloyd, G. O.; Wharmby, M. T.; Facq, S.; Cheetham, A. K.; Redfern, S. A. T. Phase Transitions in Zeolitic Imidazolate Framework 7: The Importance of Framework Flexibility and Guest-Induced Instability. *Chem. Mater.* **2014**, *26*, 1767–1769. https://doi.org/10.1021/cm500407f.

(50) Singla, P.; Luxami, V.; Paul, K. Benzimidazole-Biologically Attractive Scaffold for Protein Kinase Inhibitors. *RSC Adv.* **2014**, *4*, 12422. https://doi.org/10.1039/c3ra46304d.

(51) Osmaniye, D.; Evren, A. E.; Sağlık, B. N.; Levent, S.; Özkay, Y.; Kaplancıklı, Z. A. Design, Synthesis, Biological Activity, Molecular Docking, and Molecular Dynamics of Novel Benzimidazole Derivatives as Potential AChE/MAO-B Dual Inhibitors. *Arch. Pharm. (Weinheim).* **2022**, *355*. https://doi.org/10.1002/ardp.202100450.

(52) Lan, G.; Fan, Y.; Shi, W.; You, E.; Veroneau, S. S.; Lin, W. Biomimetic Active Sites on Monolayered Metal–Organic Frameworks for Artificial Photosynthesis. *Nat. Catal.* **2022**, *5*, 1006–1018. https://doi.org/10.1038/s41929-022-00865-5.

(53) Pohanka, M. The Piezoelectric Biosensors: Principles and Applications, a Review. *Int. J. Electrochem. Sci.* **2017**, *12*, 496–506. https://doi.org/10.20964/2017.01.44.

(54) Afzal, A.; Mujahid, A.; Schirhagl, R.; Bajwa, S.; Latif, U.; Feroz, S. Gravimetric Viral Diagnostics: QCM Based Biosensors for Early Detection of Viruses. *Chemosensors* **2017**, *5*, 7. https://doi.org/10.3390/chemosensors5010007.

(55) Lim, H. J.; Saha, T.; Tey, B. T.; Tan, W. S.; Ooi, C. W. Quartz Crystal Microbalance-Based Biosensors as Rapid Diagnostic Devices for Infectious Diseases. *Biosens. Bioelectron.* **2020**, *168*, 112513. https://doi.org/10.1016/j.bios.2020.112513.

(56) Pohanka, M. Quartz Crystal Microbalance (QCM) Sensing Materials in Biosensors Development. *Int. J. Electrochem. Sci.* **2021**, *16*, 211220. https://doi.org/10.20964/2021.12.15.

(57) P J, J.; Prabakaran, K.; Luo, J.; M G, D. H. Effective Utilization of Quartz Crystal Microbalance as a Tool for Biosensing Applications. *Sensors Actuators A Phys.* **2021**, *331*, 113020. https://doi.org/10.1016/j.sna.2021.113020.

(58) Wang, L. Metal-Organic Frameworks for QCM-Based Gas Sensors: A Review. *Sensors Actuators A Phys.* **2020**, *307*, 111984. https://doi.org/10.1016/j.sna.2020.111984.

(59) Kosuru, L.; Bouchaala, A.; Jaber, N.; Younis, M. I. Humidity Detection Using Metal Organic Framework Coated on QCM. *J. Sensors* **2016**, *2016*, 1–8. https://doi.org/10.1155/2016/4902790.

(60) Chowdhury, S.; Torad, N. L.; Ashok, A.; Gumilar, G.; Chaikittisilp, W.; Xin, R.; Cheng, P.; Ul Hoque, M. I.; Wahab, M. A.; Karim, M. R.; Yuliarto, B.; Hossain, M. S.; Yamauchi, Y.; Kaneti, Y. V. Template- and Etching-Free Fabrication of Two-Dimensional Hollow Bimetallic Metal-Organic Framework Hexagonal Nanoplates for Ammonia Sensing. *Chem. Eng. J.* **2022**, *450*, 138065. https://doi.org/10.1016/j.cej.2022.138065.

(61) Wen, Y.; Zhang, X.; Li, X.; Wang, Z.; Tang, C. Y. Metal-Organic Framework Nanosheets for Thin-Film Composite Membranes with Enhanced Permeability and Selectivity. *ACS Appl. Nano Mater.* **2020**, *3*, 9238–9248. https://doi.org/10.1021/acsanm.0c01860.

(62) Xie, B.; Yan, Y.; Wu, J.; Cai, X.; Zheng, J.; Lan, Y.; Tang, X.; Fan, J.; Zheng, S.; Cai, S. Three-Component Covalent Organic Framework Nanosheets for the Detection of MicroRNAs. *Crystals* **2022**, *12*, 1628. https://doi.org/10.3390/cryst12111628.

(63) Sauerbrey, G. Verwendung von Schwingquarzen Zur Wägung Dünner Schichten Und Zur Mikrowägung. *Zeitschrift für Phys.* **1959**, *155*, 206–222. https://doi.org/10.1007/BF01337937.

(64) Adamczyk, Z.; Sadowska, M.; Żeliszewska, P. Applicability of QCM-D for Quantitative Measurements of Nano- And Microparticle Deposition Kinetics: Theoretical Modeling and Experiments. *Anal. Chem.* **2020**, *92*, 15087–15095. https://doi.org/10.1021/acs.analchem.0c03115.

(65) Reviakine, I.; Johannsmann, D.; Richter, R. P. Hearing What You Cannot See and Visualizing What You Hear: Interpreting Quartz Crystal Microbalance Data from Solvated Interfaces. *Anal. Chem.* **2011**, *83*, 8838–8848. https://doi.org/10.1021/ac201778h.

(66) Luan, Y.; Li, D.; Wei, T.; Wang, M.; Tang, Z.; Brash, J. L.; Chen, H. “Hearing Loss” in QCM Measurement of Protein Adsorption to Protein Resistant Polymer Brush Layers. *Anal. Chem.* **2017**, *89*, 4184–4191. https://doi.org/10.1021/acs.analchem.7b00198.

(67) Reviakine, I.; Johannsmann, D.; Richter, R. P. Hearing What You Cannot See and Visualizing What You Hear: Interpreting Quartz Crystal Microbalance Data from Solvated Interfaces. *Anal. Chem.* **2011**, *83*, 8838–8848. https://doi.org/10.1021/ac201778h.

(68) Tellechea, E.; Johannsmann, D.; Steinmetz, N. F.; Richter, R. P.; Reviakine, I. Model-Independent Analysis of QCM Data on Colloidal Particle Adsorption. *Langmuir* **2009**, *25*, 5177–5184. https://doi.org/10.1021/la803912p.

Graphical Abstract